

Stellar Kinematics of the Double Nucleus of M31¹

Thomas S. Statler

Department of Physics and Astronomy, 251B Clippinger Research Laboratories, Ohio University,
Athens, OH 45701, USA; tss@coma.phy.ohio.edu

Ivan R. King

Astronomy Department, 601 Campbell Hall, University of California, Berkeley, CA 94720-3411,
USA; king@glob.berkeley.edu

Philippe Crane

European Southern Observatory, Karl-Schwarzschild-Strasse 2, D-85748 Garching, Germany; and
Department of Physics and Astronomy, 6127 Wilder Laboratory, Dartmouth College, Hanover,
NH 03755-3528, USA; phcrane@vermontel.net

and

Robert I. Jedrzejewski

Space Telescope Science Institute, 3700 San Martin Drive, Baltimore, MD 21218, USA;
rij@stsci.edu

ABSTRACT

We report observations of the double nucleus of M31 with the $f/48$ long-slit spectrograph of the *HST* Faint Object Camera. We obtain a total exposure of 19,000 sec. over 7 orbits, with the $0''.063$ -wide slit along the line between the two brightness peaks (PA 42°). Careful correction of the raw data for detector backgrounds and geometrical distortion is essential. A spectrum of Jupiter obtained with the same instrument is used as a spectral template to extract rotation and velocity dispersion profiles by cross-correlation. The rotation curve is resolved, and reaches a maximum amplitude $\sim 250 \text{ km s}^{-1}$ roughly $0''.3$ either side of a rotation center lying between P1 and P2, $0''.16 \pm 0''.05$ from the optically fainter P2. We find the velocity dispersion to be $\lesssim 250 \text{ km s}^{-1}$ everywhere except for a narrow “dispersion spike”, centered $0''.06 \pm 0''.03$ on the anti-P1 side of P2, in which σ peaks at $440 \pm 70 \text{ km s}^{-1}$. At much lower confidence, we see local disturbances to the rotation curve at P1 and P2, and an elevation in σ at P1. At very low significance we detect a weak asymmetry in the line-of-sight velocity distribution opposite to the sense usually encountered. Convolving our V and σ profiles to CFHT resolution, we find good agreement with the results of Kormendy & Bender (1999), though there is

¹Based on observations with the NASA/ESA *Hubble Space Telescope*, obtained at the Space Telescope Science Institute, which is operated by AURA, Inc., under NASA contract No. NAS 5-26555.

a 20% discrepancy in the dispersion that cannot be attributed to the dispersion spike. Our results are not consistent with the location of the maximum dispersion as found by Bacon et al. (1994). Comparing with published models, we find that the sinking star cluster model of Emsellem & Combes (1997) does not reproduce either the rotation curve or the dispersion profile. The eccentric disk model of Tremaine (1995) fares better, and can be improved somewhat by adjusting the original parameters. However, detailed modeling will require dynamical models of significantly greater realism.

Subject headings: galaxies: spiral — galaxies: individual (M31) — galaxies: kinematics and dynamics

1. Introduction

The center of our neighboring spiral galaxy in Andromeda (M31 = NGC 224) has intrigued astronomers for many decades. Although the usual overexposed portrait images of “the Great Spiral” give an impression of great blandness across the entire central region, this is far from the truth. Visual observers at least as far back as Lord Rosse recognized the abrupt rise in surface brightness toward the center, to a peak that is unresolved even in the best ground-based seeing (Hodge 1992 and references therein). The photometric structure became still more intriguing when Stratoscope II showed the nucleus to be asymmetric, with its brightest point off-center with respect to the rest of the inner bulge (Light, Danielson, & Schwarzschild 1974).

Stratoscope resolution remained unsurpassed until two decades later, when Hubble Space Telescope (*HST*) imaging showed that M31’s central brightness peak was actually double (Lauer et al. 1993). In addition to a sharp peak which is clearly at the center of the isophotes farther than 1 arcsec from the center, there is a second peak with a resolved core, about half an arcsecond from the central peak along the major axis of this central region.² Because the eccentric peak was the brighter one in the *V* band in which Lauer et al. observed, they named it P1, and the more central peak P2. This turns out to be a somewhat unfortunate choice, for reasons we discuss below.

Efforts to map the rotation, velocity dispersion, and higher moments of the line-of-sight velocity distribution (LOSVD) near the center of M31 have led to further puzzles. Given the known brightness peak, perhaps it should have come as less of a surprise when Lallemand, Duchesne, & Walker (1960) discovered a rapid central rotation, which peaked at $\pm 90 \text{ km s}^{-1}$ at $3''$ on either side of the center. Later observations, profiting from better seeing and greatly improved instrumentation, have sharpened the rotation curve, to 160 km s^{-1} at $r \approx 0''.7$, and measured a central dispersion that approaches 300 km s^{-1} in the best seeing (Kormendy & Richstone 1995). Dynamical modeling

²The spatial scale is $1'' = 3.5 \text{ pc}$ for a distance of 725 kpc (Hodge 1992).

of these data now points to the M31 nucleus as one of the more likely sites for a supermassive black hole (Kormendy & Richstone 1995 and references therein).

Recently, Bacon et al. (1994) used the TIGER multi-object spectrograph, which records 400 spectra at closely spaced points, to map the kinematic fields in two dimensions. They reported that the velocity dispersion peaks at a point that coincides with neither brightness peak. The highest velocity dispersion that they found was at a point $0''.7$ from P2, in the direction away from P1. This surprising result disagrees, however, with long-slit spectroscopy by van der Marel et al. (1994), as well as with earlier work by Kormendy (1988), both of which showed the dispersion maximum coinciding with P2 to within the angular resolution. To further complicate matters, the latter authors found a displacement of the center of the rotation curve away from P2, in the direction *toward* P1.

An interesting effort to decompose the LOSVD in the P1–P2 region into discrete kinematic components was undertaken by Gerssen, Kuijken, & Merrifield (1995) using long-slit spectra. They detected an asymmetric tail extending to positive velocities. Modeling the LOSVD as a sum of two Gaussians, they argued that the lower-amplitude, higher-velocity component should be identified with P1. Gerssen et al. did not go so far as to assert that P1 actually is a distinct physical component. However, Emsellem & Combes (1997), modeling the TIGER data, have vigorously advocated a model in which P1 is a dense star cluster on the verge of tidal disruption by the central black hole.

The mystery deepens still more when we look at the population characteristics of the two peaks of brightness. As shown by King, Stanford, & Crane (1995), P2 increases in brightness at shorter wavelengths, whereas P1 has the same color as the surrounding bulge light, from the far ultraviolet to the near infrared. Lauer et al. (1998), using post-repair *HST* imaging, show that P2 is bluer than its surroundings throughout the optical range of wavelengths, and in addition find that P2 has a resolvable core profile. The color properties of both P1 and P2 are surprising. The changing color of the dynamical center P2 suggests the presence of some other source of radiation in addition to the stars that make up the bulge. Even more perplexing, however, is the color of P1. The interpretation of such an object as a large globular cluster or a small dwarf elliptical galaxy is tempting, but the colors militate against this. Either a globular cluster or a dwarf elliptical would be expected to have a metallicity considerably below solar, whereas the color of P1 is, over a large range of wavelength, a near-perfect match to the color of its surroundings, which have a metallicity that is above solar.

Tremaine (1995) suggested an ingenious model that, in principle, could simultaneously solve the population dilemma of P1 and explain the nuclear kinematics. The essence of the model is that P1 is not a self-bound object, but only a statistical accumulation of stars near the apocenters of their orbits in an eccentric Keplerian disk surrounding the black hole, which lives within P2. Tremaine was able to produce an excellent fit to the Lauer et al. (1993) photometry and Kormendy's (1988) kinematics. While the question of how to form such a disk in a galactic nucleus is far from

trivial, it is at least possible that the configuration, once formed, could be long lived, in contrast to models where P1 is a bound object on the brink of destruction.

The high spatial resolving power of *HST* has already led, as indicated above, to a sharper knowledge of the spatial properties of the nuclear region of M31. In this paper we investigate the kinematics with a similarly improved resolution. Our presentation is organized as follows: In Sec. 2 we describe the long-slit capabilities of the *HST* Faint Object Camera and our observational program. Issues of data reduction, which are substantial, are discussed in Sec. 3. Sec. 4 describes the methods used to extract the kinematic profiles and presents the results. In Sec. 5 we compare the kinematics as revealed by the FOC with groundbased data and with the published dynamical models. Finally, we summarize the main results in Sec. 6.

2. Observations

2.1. The $f/48$ Spectrograph

Until the installation of STIS, the only long-slit spectrograph on board *HST* was in the Faint Object Camera. In the planning of that instrument, the members of its Instrument Science Team had realized that the $f/48$ camera of the FOC could be given a spectrographic capability if a grating were installed in such a position that temporary insertion of a diverting mirror into the light beam sends the latter to the grating before it reaches the cathode. The diverting mirror and grating are tilted by a small amount, so that what this optical mode images onto the cathode is not the usual imaging aperture but rather a long slit that is just to the side of the imaging aperture.

The spectrograph slit measures 0.063×12.5 arcsec. Spectra are recorded over the wavelength range 3600 to 5400 Ångstroms, on a field that extends 1024 pixels in the dispersion direction and 512 pixels in the spatial direction; of the latter, 446 pixels cover the slit length. Each pixel is $50 \times 25 \mu\text{m}$ in size ($56 \text{ mas} \times 1.7 \text{ Å}$).

The image of the slit is 2.3 pixels wide on the cathode, thus degrading the spectroscopic resolution in return for an increased throughput. (This width was chosen by IRK and PC, as members of the IST, specifically with the present program in mind.)

2.2. Planning of the Program

This program (GTO-6255) was part of the Guaranteed Time Observations (GTO) of IRK. In the division of GTO orbits between various projects, it was assigned 9 orbits, of which 7 were to be used for the actual spectroscopic exposure. Calculations of surface brightness and instrumental sensitivity had indicated that this exposure length would produce an adequate spectrum, at least in the brightest central region. The position angle chosen for the slit was 42° , which would lay it

across P1 and P2.

It had been planned to carry the program out much earlier, but the $f/48$ camera failed in 1992 and was unusable for more than 2 years. When it unexpectedly came back to life in 1995, the program was reactivated and carried out. Unfortunately the revived $f/48$ had problems of background noise; to monitor these we took a flatfield image (using an internal light source) and a dark image (shutter closed) during each occultation period. As we shall see below, the background anomalies varied with time in such a way that we were unable to remove them completely.

After beginning the reductions, we found that data for wavelength calibration were lacking; in particular, we needed to determine the dependence of the wavelength scale on position along the slit. Furthermore, it quickly became apparent that it would be impossible to extract reliable kinematic profiles without a stellar spectral template of approximately the right spectral type, observed with the same instrument. IRK and RIJ therefore prepared a calibration program (CAL/FOC-6926) which secured a well-exposed spectrum of Jupiter, with the planet covering nearly the entire length of the slit. Because of the danger of undispersed light of Jupiter coming through a direct path that exists in the spectrograph, this exposure had to be made at the limb of Jupiter's disk. Thanks largely to the absence of absorption bands in the visible from the main constituents of the Jovian atmosphere, the result was essentially a reflected solar (G2) spectrum.

2.3. Acquisition

M31 was observed during 10 orbits of *HST* on 4–5 December 1995 UT. The first orbit was devoted to the direct imaging of the target that is required for every pointing of the spectrograph slit. This image is downlinked to the observer, who indicates where the slit should be placed. A pointing change is then made that should place the slit correctly. Unfortunately, however, the location of the slit relative to the imaging format was not well enough known to place it precisely across the centers of P1 and P2. We therefore took five exposures of 357 s each over the next two orbits, displacing the slit laterally by $0''.05$ each time, and each of these was downlinked as soon as it was complete. We collapsed each of these images in the dispersion direction, so as to provide a brightness profile, and we used the intensities of these to judge where the center of M31 lay, among the 5 positions. We believe that our chosen position, at which the slit was held for the next 7 orbits, is within $0''.05$ of the center of M31.

The total exposure in those 7 orbits was 19,097 s.

3. Data Reduction

3.1. Cleaning

The raw FOC data contained a number of artifacts introduced by the detector that hampered our original efforts at processing. These included: remnants of the detector fly-back, burn-in lines on the photo-cathode, and analog-to-digital converter glitches, to mention a few. In addition to these, which are primarily high-spatial-frequency perturbations, there were also two larger artifacts: an arc extending over nearly a quadrant, and a diffuse flare near the center, with a diameter of more than 200 pixels. These were of course of lower spatial frequency, and varied with time. We developed a simple procedure that was able to remove most of these artifacts; and, most importantly, the process removed those high-spatial-frequency features which would affect our analysis of the absorption lines most severely.

We had eight dark frames available, taken in the occultation periods before and after the data frames. The cleaning process made use of these darks in the following manner: (1) The dark frames were summed directly using the relevant IRAF task. (2) The resulting image was edited to remove the most obvious high-frequency features. Image editing was preferred over a low-pass filtering technique. (3) The edited image was gaussian-smoothed using a symmetric gaussian with $\sigma = 5$. (4) The smoothed image was subtracted from the original summed dark image. The resulting background frame now had the high frequency artifacts emphasized. (5) This background frame was scaled using an empirically determined scaling factor, and subtracted from the individual data frames. The scaling factors were determined individually for each data frame, since the artifacts varied from frame to frame. The dark-subtracted images were then further processed as described in the following section.

This rather simple procedure produced images that, although not perfect to look at, gave considerably more reproducible results when analyzed. It took several iterations on several versions of the data before we realized that the first step in the process should be this cleaning, before the geometrical correction.

3.2. Flattening and Geometrical Corrections

The raw data from the $f/48$ camera consisted of a 512×1024 array of pixels approximately $50 \times 25 \mu\text{m}$ in size (the so-called “zoomed” pixel format). The first step was to “dezoom” the image by replacing each $50 \times 25 \mu\text{m}$ pixel with two $25 \times 25 \mu\text{m}$ pixels, each with half of the flux of the zoomed pixel. This made the resultant image a 1024×1024 -pixel square.

The FOC suffers from geometric distortion as a result of the electric and magnetic fields used to focus the electron beam that is produced when a photoelectron is detected at the photocathode. There is additional distortion that arises from the spectrograph optics. The geometric correction process had to remove this distortion and deliver an image in which lines of constant wavelength are horizontal (wavelength independent of position x along the slit) and points at a given location

along the slit trace a vertical line (spatial position independent of y coordinate in the dispersion direction).

In the raw dezoomed data, lines of constant wavelength were tilted by approximately 7° to the horizontal, and lines of constant position along the slit were approximately 8° to the vertical. The nonlinear nature of the geometric distortion made these tilts functions of position on the detector. The nonlinear distortion could be removed by using the grid of reseau marks evaporated onto the photocathode; these spots, approximately $75\ \mu\text{m}$ in size and forming a regular grid with spacing exactly 1.5 mm, were easily visible in internal flatfield images.

A description of the calibration of FOC spectrograph data is given in Voit (1996) and in Jedrzejewski & Voit (1997). Spectra of the planetary nebula NGC 6543 were used to regularize the emission lines (lines of constant wavelength), and spectra of a star at two positions along the slit were used to map the distortion in the spatial direction. The star was imaged both near the center of the slit and $3''$ along the slit in the direction away from the imaging format. The geometrical correction that made the trace of the star in the first spectrum exactly vertical also rectified the second spectrum to a good approximation. From this we deduced that the distortion was not dependent on the position of the object on the slit. The expense of these calibration exposures in telescope time precluded a more careful mapping of the distortion.

Unfortunately, the geometric distortion in the FOC changes with time in an unpredictable way, with typically a slight rotation of the field of a few tenths of a degree over several orbits, and changes in the effective plate scale of a few tenths of a percent over the same period. This means that the transformation used to correct the calibration data was not applicable to the science data described here; the time-dependent distortions are not removed. However, the correction for the geometric distortions transforms the reseau marks to a well-defined set of positions. Non-calibration FOC spectra can therefore be corrected by transforming the data so that the reseau marks are transformed into the positions of the marks in the optimally calibrated data. Having taken internal flatfields in the occultation periods between the M31 science exposures, we were able to measure the coordinates of the reseau marks that correspond in time with the science data and then generate custom geometric correction reference files to remove the time-dependent component of the distortion. Using this method gave geometrically corrected spectra with only one resampling of the data, preserving most of the information on the smallest scales. It also allowed the re-transforming of the data to take account of small single-orbit shifts of the spectra, as described in Section 3.3. Thus the geometric transformations and the positional shifts could be done in a single pass, and the only further resampling needed was the conversion to a logarithmic wavelength scale, which was done after wavelength calibration (Sec. 3.4).

Conventional flatfielding, such as is applied to direct images, was not carried out. First, no spectroscopic flatfield exists; second, conventional flatfielding, as carried out for the FOC, affects only low spatial frequencies that play no role in the work that we are doing here.

3.3. Registration

After correction for geometrical distortions, the single-orbit spectra were still not positioned identically on the detector. The displacements must arise within the spectrograph rather than from a shift in telescope pointing, as they exist both in the spatial (x) direction and in the wavelength (y) direction. We believe that the errors originate from the removable spectrograph mirror, which had to be removed during each occultation period for the flatfield and dark exposures, and then replaced for the M31 spectrographic exposure. We believe that the mirror fails to seat exactly the same each time.

The relative offsets in the spatial (x) direction were computed by TSS by summing the spectra in the y direction over the central 800 lines to obtain 1-dimensional spatial profiles, then cross-correlating these against each other. The spatial offsets were also determined independently by IRK in a similar way that differed only in detail; the results were in agreement within a few tenths of a pixel. The offsets in the wavelength direction were calculated by TSS as part of the wavelength calibration, as described below.

3.4. Wavelength Calibration

The FOC spectrograph contains no internal arc lamps for wavelength calibration; moreover, the instrument has been so little used that there are no contemporaneous observations of emission-line sources that could be used for the same purpose. Therefore, we used a ground-based spectrum of M31, obtained by Ho, Filippenko, & Sargent (1993, hereafter HFS) with the Hale 5 m and kindly provided to us by Luis Ho and Alex Filippenko, to calibrate both the M31 and Jupiter spectra. This differed from the straightforward approach, which would have been to derive a wavelength scale from identified lines in the Jupiter spectrum and assume that the same scale applied to M31. We chose to calibrate the M31 spectrum independently as a consistency check. Below we describe the method used to perform this calibration with the groundbased spectrum. This method subsequently proved to be very robust in calibrating the Jupiter spectrum, and superior to a “traditional” line-ID approach. Thus both galaxy and template spectra are calibrated to the HFS spectrum, which consequently defines the velocity zero point for our derived kinematics.

The 2"-wide slit (at position angle 77°) used by HFS projects, at our slit PA of 42° , into a 3.5" length along our slit, corresponding to 125 of our columns. Thus from each of the individual x -shifted M31 frames we extracted a 125-column sum centered on P2. Since this included the entire well-exposed part of the spectrum, the final calibration was not sensitive to the chosen width. Each resulting 1-D spectrum was then matched to the HFS spectrum using a two-parameter cross-correlation. That is, given the HFS spectrum $S(\lambda)$ and the uncalibrated spectrum $G(y)$, we assumed a mapping from pixel number to wavelength of the form $\lambda = ay + b$. We then computed

$$\xi(a, b) = \int S(\lambda)G\left(\frac{\lambda - b}{a}\right) d\lambda, \quad (1)$$

and maximized with respect to a and b . For the individual frames a and b were not well constrained separately, but a linear combination of them was, and its slope was nearly the same for all frames. We could therefore obtain the relative offsets of the spectra by comparing the best-fit b values at fixed a . We chose to do this at $a = -1.7 \text{ \AA/pixel}$; for $-1.69 \leq a \leq -1.71$ the derived offsets differed by < 0.3 pixel. (Negative a means merely that the short-wavelength end of the spectrum was at the high-pixel-number end of the detector.)

To reduce the effects of accumulated roundoff error in rebinning the images, the complete set of geometrical corrections, including the x and y offsets, was then re-done in a single pass. The seven resulting frames were co-added, and $\xi(a, b)$ recomputed for the same 125-column sum. With the higher S/N of the co-added spectrum, a was much better constrained, the best-fit value being $-1.7012 \text{ \AA/pixel}$. All subsequent analysis was performed on the wavelength calibrated co-added spectrum in de-zoomed format. Even though the individual exposures contained no information on scales smaller than the zoomed pixels, the time-variable geometric distortions (Sec. 3.2) and image shifts (Sec. 3.3) produced an unintentional, though beneficial, dithering on the detector, so that some of the higher resolution can be recovered in the co-added image. Still, features smaller than two de-zoomed pixels wide should be treated with some skepticism.

The three individual exposures of Jupiter were summed in the spatial direction, avoiding reseau marks and cosmetic defects. The 1-dimensional spectra were of sufficiently high S/N that the residual y shifts could be determined by eye to within 0.1 pixel. The shifted spectra were then coadded. Wavelength calibration was slightly complicated by the radial velocity difference between Jupiter and M31. In calculating $\xi(a, b)$ the Jupiter spectrum was Doppler shifted (*i.e.*, logarithmically in wavelength) to an assumed velocity $v_J - v_{\text{M31}} = -300 \text{ km s}^{-1}$ before integrating. Otherwise, calibration was done as described above, with the result $a = -1.7017 \text{ \AA/pixel}$. There was no sign of a need for a higher-order term in the wavelength solution. The 0.03% difference between this value of a and that obtained from the M31 data is insignificant. Owing to the higher S/N in the Jupiter spectrum, and since the larger value of a is still consistent with the M31 spectrum, we adopted this result for both.

Because the calibrated Jupiter spectrum was blueshifted to the velocity of the HFS spectrum, all velocities in this paper are measured relative to the HFS mean, which is an average over an 8 arcsec^2 aperture centered on the nucleus. Residual calibration errors may introduce a systematic offset in the velocity scale; however, we believe any such offset should be $< 50 \text{ km s}^{-1}$. Mean errors in the y registration offsets of ~ 0.3 pixel would generate a $\sim 35 \text{ km s}^{-1}$ systematic error in velocity dispersion, which would add in quadrature. Our derived dispersions are substantially above 100 km s^{-1} , so this is not likely to be a significant effect.

4. Stellar Kinematics of the Double Nucleus

4.1. Methods & Strategies

The best-exposed section of the co-added M31 spectrum is shown in Figure 1. The figure covers the region from about 3670 Å to 5500 Å, and extends 6'' either side of P1 and P2, which produce the parallel streaks down the middle of the image. Ca II H+K are easily visible near the top, and, less conspicuously, the G band, H β , Mg b , and a number of weaker lines. Also visible are residuals from the incomplete subtraction of the arc and flare and imperfectly cleaned cosmetic defects. The S/N ratio reaches no higher than 14 (per pixel) at the centers of P1 and P2, making the extraction of the stellar kinematics challenging. For comparison, one generally aims for $S/N \gtrsim 20$ in ground-based absorption-line work to derive mean velocities and dispersions, and $S/N > 30$ to obtain higher moments. Furthermore, in this case we could not substantially increase S/N by coarse spatial binning since the noise is dominated by background systematics.

Nonetheless, even a casual inspection of H+K shows clear rotation in the double nucleus. Lulled into false confidence by the Ca lines, we proceeded with the kinematic analysis, only to meet with disappointing—as well as borderline unphysical—results. After a good deal of wasted effort we realized that Ca II H+K were being contaminated by residual background from the arc, and the correlation signal corrupted by the disproportionate contribution of these two strong lines. The results improved dramatically when we discarded the Ca lines and relied on the combined signal from the much more numerous weak lines in the spectrum.

The region of the final image used in our subsequent analysis is marked by the box in Figure 1. One-dimensional spectra extracted from this region were divided by continua fitted using high-order cubic splines. They were then rebinned onto a logarithmic wavelength scale with 833 bins between 3984.39 Å and 5453.00 Å, corresponding to a velocity scale of $113.06 \text{ km s}^{-1} \text{ pixel}^{-1}$. The same was done for the Jupiter spectrum.

Because S/N was far too low to allow nonparametric extraction of the LOSVD, we assumed Gaussian broadening functions and recovered the mean velocity V , dispersion σ , and normalization (“line strength”) γ using Statler’s (1995) implementation of the cross-correlation method. (We deal with the h_3 and h_4 Gauss-Hermite coefficients in Section 4.4.) The cross-correlation method exploits the following identity: if the galaxy spectrum G is the convolution $S \otimes B$ of the stellar template spectrum S and the broadening function B , then the galaxy-template cross-correlation function, $X = G \circ S$, and the template autocorrelation function, $A = S \circ S$, are related by $X = A \otimes B$. In our implementation, a region of specified width around the primary cross-correlation peak is fitted with a parameterized B convolved with A , and the parameters are manipulated to optimize the fit. For high S/N data the results are not very sensitive to the size of the fitting region; however, this becomes an important issue for the present data.

Prior to cross-correlating, galaxy and template spectra were filtered in the Fourier domain to remove low-frequency components. The filter was zero below a threshold wavenumber k_L (measured in inverse pixels), unity above $2k_L$, and joined by a cosine taper in between. It is convenient to give the filter width W_T in Fourier-space pixels, in terms of which $k_L = W_T/833$.

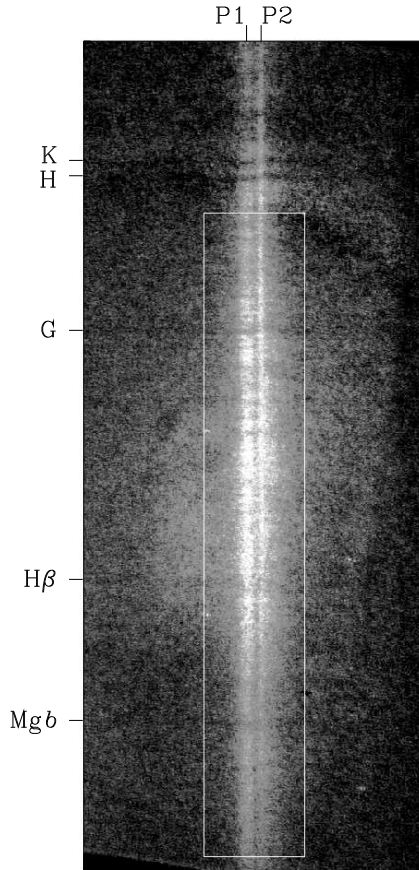


Fig. 1.— Final cleaned, geometrically corrected, co-added spectrum of the M31 nucleus. The spectrum runs from $\sim 3670 \text{ \AA}$ at the top to $\sim 5500 \text{ \AA}$ at bottom. Bright vertical streaks are P1 (left) and P2 (right). Ca II H+K are easily visible near the top; the G band, H β and Mg b are less conspicuous. Note the residual smooth unsubtracted background and the curved residual “arc” feature that contaminates H+K. White box shows the section of the spectrum used for the kinematic analysis.

The correlation peaks at five points along the slit, computed with $W_T = 10$, are shown in Figure 2. The point at $-0''.49$ is the center of P1. (All distances are measured with respect to the P2 brightness maximum.) The point at $+0''.36$ is approximately symmetrically placed on the other side of the rotation curve center; comparison shows a clear velocity difference of $\sim 450 \text{ km s}^{-1}$. On top of the data are plotted the fitted curves, $X_{\text{fit}} = A \otimes B_{\text{fit}}$, where the fits are confined to windows within $\pm W_{\text{fit}}$ pixels of the maximum of X . We show the results for $W_{\text{fit}} = 2, 3, 5, 7, 9, 11$. At $-0''.49$ and $+0''.36$ the results are very robust, as all the fitted curves fall on top of each other. At $-0''.207$, in the brightness minimum between P1 and P2, S/N has come down a bit and the wings of the correlation peak are less reliable; but again the inferred V and σ are still insensitive to the fitting width W_{fit} . This is typical of the entire spectrum between $-1''.0$ and $+0''.4$, *except* for a very small region about $0''.25$ wide centered near P2. The remaining two frames in Figure 2

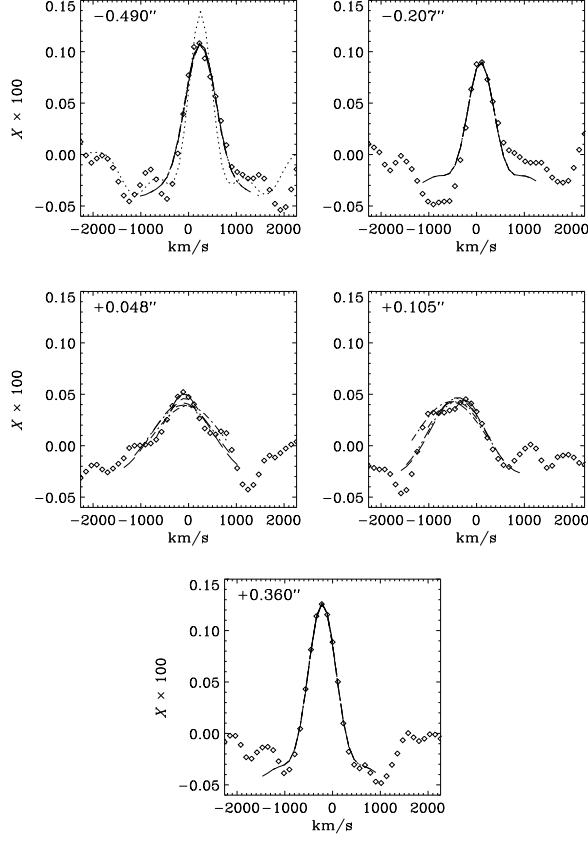


Fig. 2.— Primary peaks in the M31–Jupiter cross-correlation functions (*points*) for galaxy spectra at five points along the slit, computed with a filter width $W_T = 10$ (see Sec. 4.1). Positions are given relative to P2. Overplotted (*smooth curves*) are the fitted functions obtained by convolving the template autocorrelation function (*dotted line* in the first panel) with the LOSVD. Different line styles show results of confining the fit to windows within $\pm W_{\text{fit}} = 2, 3, 5, 7, 9, 11$ pixels of the maximum of X . The results are sensitive to W_{fit} only in the region of the dispersion spike (*middle two panels*); however, even the smallest window gives values of σ substantially higher than away from the spike.

show the correlation peaks at two points near the center of this region. These points are separated by one “zoomed” pixel width, approximately 1 FWHM of the PSF, so the data are essentially independent. The correlation peaks have clearly broadened out and come down in amplitude. The maximum amplitude is now comparable to that of noise features,³ and it is difficult to tell what the real extent of the peak is. As a result, the fitted X_{fit} depends sensitively on the width of the fitting window.

To gain some control over this systematic uncertainty, we exploited the well known covariance

³Remember that errors in the cross-correlation function are strongly correlated, so smooth-looking features can result from noise in the spectra.

between velocity dispersion and line strength common to all LOSVD fitting methods. A normalized Gaussian has a central amplitude proportional to σ^{-1} , and inspection of Figure 2 shows that the amplitude of X comes down in the exceptional region by about a factor of 2. If there is no variation in the intrinsic line strength, this would indicate about a factor 2 increase in dispersion. In the plotted examples we obtain lower dispersion ($\sim 340 \text{ km s}^{-1}$) for small W_{fit} since only the top part of the peak is fitted, but the fit also requires a low γ (~ 0.5) to pull the amplitude down to match the data. Similarly, wide W_{fit} gives large σ and large γ . Over the rest of the spectrum between $-1''.0$ and $+0''.4$ the value of γ is quite stable, with an average of 1.02. We therefore decided to constrain σ by *assuming* that there is no significant variation in γ in this small region. We ran the correlation analysis over a grid of filter widths ($W_T = 8, 10, 12, 15, 18$) and fitting widths ($W_{\text{fit}} = 2, 3, 5, 7, 9, 11$), and took a weighted average of the results. The weights for each point i in the (W_T, W_{fit}) grid were set independently at each point along the slit, according to $w_i = \exp [-(\gamma_i - 1.02)^2 / (2s^2)]$. The width s was set to 0.1, exponentially excluding combinations of W_T and W_{fit} giving more than a 10% variation in γ .

An additional complication to this strategy is the unsubtracted smooth background still present in the final spectrum. This should enter as essentially an additive constant, lowering the line strength by a multiplicative factor and leaving the dispersion unchanged. We have not attempted to correct for this effect explicitly since the background is a relatively minor contribution in the P1–P2 region and the model-dependent correction could tend to overemphasize regions of higher dispersion.

Pushing out to larger radii proved to be very difficult, and we found that even semi-objective strategies like the one just described behaved badly. We were forced simply to choose $W_{\text{fit}} = 2$ in order to keep the dispersion consistently low enough to agree with existing groundbased data. We took an unweighted mean of the results using $W_T = 8, 10, 12, 15$, and obtained outer kinematic profiles that are at least consistent with the expected behavior of V and σ around $2''$ from the center. However, we do not have a great deal of quantitative confidence in our results for this region, and we plot them with different symbols in the figures below.

4.2. Rotation and Dispersion Curves

Our results for the nuclear rotation curve and dispersion profile are shown in Figure 3. In the top panel, the approximate surface brightness profile along the slit is shown for orientation. This is merely the integral of the un-flux-calibrated spectrum over wavelength. We have subtracted a constant background level of 0.25 of the maximum to compensate for the residual smooth background and to approximately fit the Lauer et al. profile. P1 and P2 appear here to be of comparable brightness, even though P1 is substantially brighter in the V image of Lauer et al. (1993). This is attributable to color differences between the two peaks (King et al. 1995, Lauer et al. 1998); P2 is actually brighter than P1 shortward of about 4300 Å. The second panel shows the constrained line strength γ . Recall that we are forcing the γ profile to be flat between $-0''.95$ and $+0''.4$, so this

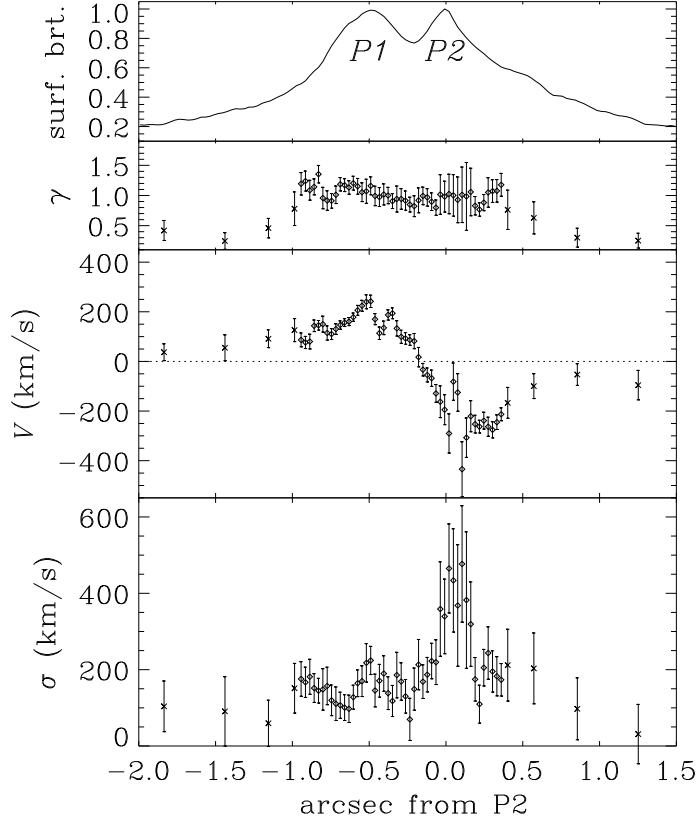


Fig. 3.— M31 nuclear rotation curve and dispersion profile, at “de-zoomed” pixel resolution. *Top panel*, approximate surface brightness profile along the slit. *Second panel*, constrained line strength parameter γ . (This is *not* an actual measurement of line strength; see Sec. 4.1). *Bottom two panels*, rotation curve and dispersion profile. *Diamonds* show the best data, to which γ -weighted averaging has been applied. *Crosses* indicate radially-summed data for which no such averaging was feasible and which are prone to large systematic errors.

is *not* a measurement of the line strength; it should be read as an indicator of systematic errors. Note that at larger radii (crosses) γ falls, partly as a result of the narrow fitting window, and partly because of the unsubtracted background.

The noteworthy features of the V and σ profiles, in order of decreasing certainty, are:

1. The velocity zero crossing is between P1 and P2, $0.^{\circ}16 \pm 0.^{\circ}05$ from P2. We will refer to this point as the rotation center (RC).
2. The rotation curve through RC is resolved; the projected velocity gradient at RC is approximately $300 \text{ km s}^{-1} \text{ pc}^{-1}$ (for an assumed distance of 725 kpc).

3. Except for small regions near P1 and P2, the rotation curve is essentially symmetric about RC, with maximum amplitude $\sim 250 \text{ km s}^{-1}$ reached about $0''.34$ from RC.
4. The velocity dispersion is $\lesssim 250 \text{ km s}^{-1}$ everywhere except for the small region, $0''.25$ wide, centered $0''.06 \pm 0''.03$ past P2, which we call the dispersion spike.
5. The maximum σ in the dispersion spike is $440 \pm 70 \text{ km s}^{-1}$.
6. There may be a disturbance to the rotation curve at P1 which has the signature of a marginally resolved local rotation in the same sense as the general rotation of the nucleus.
7. There may be a slight elevation in σ at P1.
8. There may be a large unresolved feature in the rotation curve within the dispersion spike.

4.3. Further Tests

The most striking feature in the kinematic profiles is the dispersion spike. We performed several additional tests to verify that it is real.

First, we summed pairs of columns in the de-zoomed image to increase S/N and repeated the kinematic analysis at half the spatial resolution (that is, going back to the original zoomed pixel size). The double-binned kinematic profiles are shown in Figure 4. All of the major features of Figure 3 are reproduced, including the dispersion spike. Marginal features that are unresolved at single-column resolution are smoothed over by the coarser binning.

Second, we double-binned the de-zoomed single-column spectra to half the *spectral* resolution and again re-did the analysis. This produced essentially the same cross-correlation peaks as the examples shown in Figure 2, but sampled at twice the original spacing. The broadening of the peaks in the region of the dispersion spike was not affected.

Third, to test whether the spike could be the result of a locally contaminated region of the image (like the contamination of Ca H+K discussed above), we broke the spectrum into red and blue halves and again repeated the analysis. To preserve a workable S/N ratio it was necessary to work with the double-summed columns. Once again the kinematic profiles were qualitatively unchanged.

Finally, concerned whether an error in registration or some other unrecognized single-frame problem could be producing a spurious feature, we constructed 7 co-adds of 6 of the frames, excluding each one in turn. As before, the kinematic profiles were not significantly affected.

We should emphasize that, although the amplitude of the spike depends on the cross-correlation fitting width W_{fit} , the spike is still present even when only the narrowest, most sharply curved section of the correlation peak is fitted. And while it is possible that our results for P2 could be

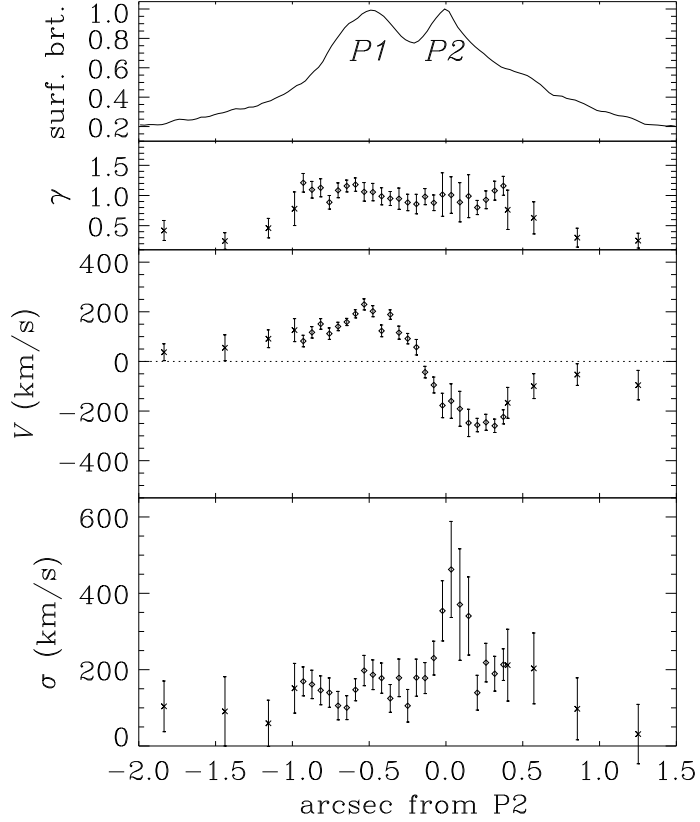


Fig. 4.— Same as Figure 3, but with the best data double-binned to the original “zoomed” pixel scale.

affected by its unresolved center behaving effectively as a point source in our relatively wide slit, point-source contamination would tend to make the line profile narrower, not broader.

As a result of these tests, we believe that the dispersion spike is a real feature, and that at least items 1–5 in our list above accurately describe the stellar kinematics of the nucleus.

4.4. Gauss-Hermite Terms

The higher moments of the LOSVD are potentially important constraints on models of the nuclear dynamics. Unfortunately, we have insufficient signal to be able to recover these quantities at anything but the coarsest of resolutions. We broke the best-exposed region into two $0''.53$ (19-column) bins on either side of the RC and extracted the LOSVD using a Gauss-Hermite expansion for the broadening function (van der Marel & Franx 1993, Statler 1995), truncated at fourth order. The h_3 and h_4 coefficients are related, respectively, to the skewness and kurtosis of the LOSVD.

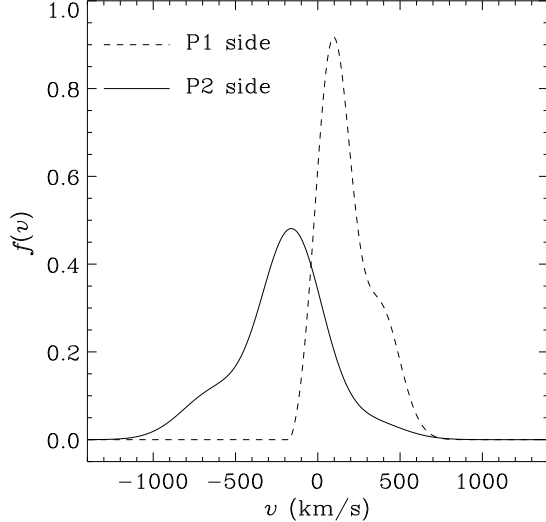


Fig. 5.— LOSVDs reconstructed from the derived V , σ , h_3 , and h_4 parameters for spectra summed over two wide radial bins on either side of the rotation center. The wide wings on the P2 side are consistent with the shapes of the correlation peaks in the dispersion spike (Fig. 2). The h_3 values, nonzero at marginal significance, suggest a longer tail to the velocity distribution in the direction of rotation, opposite to sense of skewness generally seen.

The results again depend on the filter and fitting-width parameters. We choose W_{fit} to encompass the region between the first maxima on either side of the primary correlation peak, and adopt $W_T = 12$ simply on the grounds that this combination gives $\gamma \approx 1$. We obtain, for the P1 side, $h_3 = 0.21 \pm 0.35$, $h_4 = 0.08 \pm 0.50$, and for the P2 side, $h_3 = -0.08 \pm 0.07$, $h_4 = 0.11 \pm 0.11$ (internal errors only).

The reconstructed LOSVDs for the two sides of the rotation center are shown in figure 5. There is an indication of very wide wings on the P2 side, consistent with the visual impression of the correlation peaks in the dispersion spike. The h_3 values, while differing from zero at only marginal statistical significance, are consistently of opposite sign for all choices of W_T and W_{fit} . Note, however, that the longer tail of the distribution is in the direction of rotation, which is opposite to sense of skewness generally seen. This disagrees with the ground-based results of van der Marel et al. (1994), where V and h_3 are found to be of opposite sign, as usual; but whether their resolution would have been sufficient to resolve a change of sign of h_3 in the inner half arcsecond is not clear. We admit that this is statistically a very weak result and eagerly await confirmation by STIS.

5. Discussion

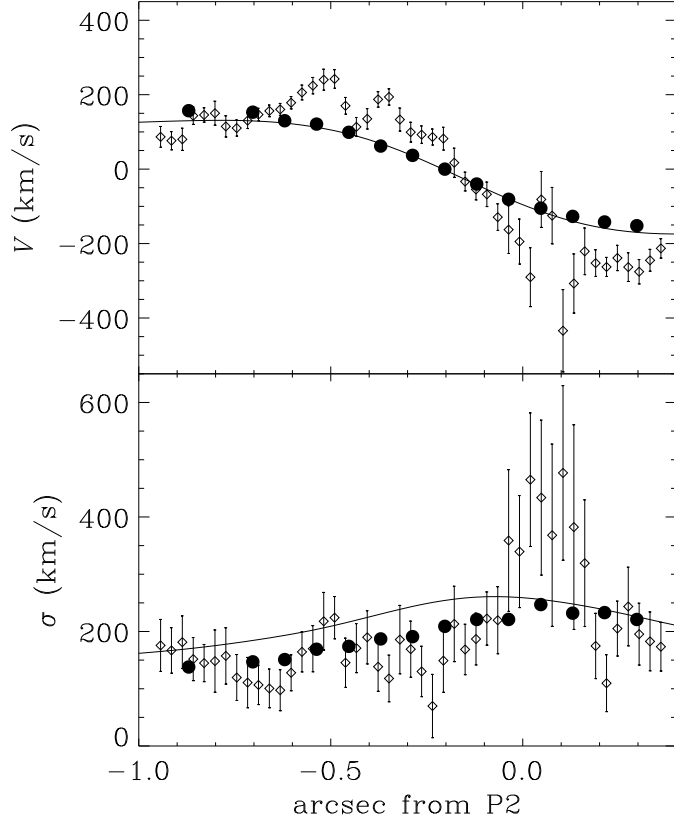


Fig. 6.— Comparison of the FOC kinematic profiles (*diamonds*) with groundbased results from CFHT/SIS (Kormendy & Bender 1999) (*circles*). *Smooth curves* show our results convolved to CFHT resolution.

5.1. Comparison with Groundbased Observations

Several recent groundbased studies have focused on the rotation and dispersion of M31’s double nucleus. None has been able to resolve the central rotation curve, and none has reported a velocity dispersion spike of the magnitude we see near the position of P2. In this section we address whether our results (Figures 3 and 4) are consistent with the lower-resolution groundbased data.

The highest-resolution groundbased work to date is that of Kormendy & Bender (1999, in preparation; hereafter KB), some results of which are presented by Kormendy & Richstone (1995). KB used the Canada-France-Hawaii Telescope Subarcsecond Imaging Spectrograph with a $0''.353$ -wide slit, in $0''.63$ seeing (FWHM). The kinematic results from their non-bulge-subtracted spectra (read directly from Figure 7 of Kormendy & Richstone 1995) are plotted as the filled circles in Figure 6. Our results are plotted as diamonds, and the plot is confined to the region of our best data.

To make a valid comparison between the two data sets we must convolve our data to CFHT resolution. This requires a two-dimensional convolution due to the presence of structure on scales smaller than the SIS slit. Since our slit is less than one-fifth as wide, we must make some assumptions for the structure of the nucleus in the perpendicular direction. We proceed as follows: let the coordinate on the sky in the direction of the slit be x and the perpendicular coordinate be y . First we build a smooth 2-D model for the surface brightness distribution, $\mu(x, y)$, that merges our 1-D spatial profile with the Lauer et al. (1993) V -band image. The model reproduces the Lauer et al. isophotes to within ~ 0.2 magnitude, and as the results are not sensitive to the details of the model, there is nothing to be gained from a more exact fit. We extrapolate our V and σ profiles to large x (beyond the edge of the plot in Figure 6) by tacking the KB profiles onto the end of our data. Since features beyond a few tenths of an arcsecond are resolved by KB, this makes little difference to the convolved profiles in the inner region, and eliminates any influence of our very uncertain results for larger radii. We extrapolate the mean velocity field in the y direction by assuming no dependence on y ; in other words, equal-velocity contours are straight lines perpendicular to the slit. We do the same for the dispersion field, except for the dispersion spike, which we assume to be round, σ falling with y to an ambient value of 180 km s^{-1} . We then convolve the three velocity moments, μ , $\mu\langle v \rangle$, and $\mu\langle v^2 \rangle$, with an analytic fit to the PSF provided by John Kormendy, and, at each x , integrate over a $0''.353$ wide boxcar window in y . Finally, we recover the mean V and dispersion σ from the convolved moments.

The resulting rotation curve, convolved to CFHT resolution, is shown as the smooth curve in the top panel of Figure 6. (Because the spatial origin in the KB data is defined to be the center of the rotation curve, we have shifted both KB profiles to match the velocity zero point of our convolved rotation curve.) The velocity gradient near the RC is reproduced extremely well; and while there is some disagreement $\gtrsim 0''.5$ from P2, where our curve is $\sim 30 \text{ km s}^{-1}$ higher than KB's on the P1 side and $\sim 20 \text{ km s}^{-1}$ lower on the anti-P1 side, this is consistent with the likely level of systematic error in our velocity zero point. In our judgment, the FOC rotation curve is completely consistent with the KB data.

Our convolved dispersion profile is plotted as the smooth curve in the bottom panel of Figure 6. Notice that at CFHT resolution the dispersion spike all but disappears; the maximum dispersion in our convolved profile is only about 5% higher than KB's peak value, and occurs only $0''.12$ from KB's peak, which is consistent with zero at their resolution. The only significant disagreement in the dispersion profiles is that ours is systematically high by about 50 km s^{-1} on the P1 side of P2. This is *not* attributable to the dispersion spike. The convolved profile does ride above most of our unconvolved data points, but not because of the spike, rather because of unresolved rotation. Removing the spike entirely from our data and repeating the convolution alters the profile by no more than 20 km s^{-1} , and only in the vicinity of the spike; it makes no difference in the region where the discrepancy is largest. The dispersion spike would not have been detected by KB, because, at a characteristic size $\sigma_{\text{spike}} \approx 0''.1$, it is substantially smaller than KB's $\sigma_{\star} = 0''.27$ seeing disk.

Our convolved profile could be reconciled with KB's if we were systematically overestimating

the dispersion by $\sim 50 \text{ km s}^{-1}$. We suspect that this may be the case, but unfortunately we have not been able to determine why. We have tested the cross-correlation code against artificial galaxy spectra made by broadening the Jupiter template, and find no tendency to overestimate σ unless $\sigma \lesssim 40 \text{ km s}^{-1}$. We have repeated these tests with a constant background level added to the artificial spectra, to simulate the smooth unsubtracted background in the final M31 spectrum, with the same result. It is possible that template mismatch could induce a systematic error of this magnitude, but, lacking other stellar spectra observed with the same instrument, we are unable to assess this effect quantitatively.

An interesting decomposition of the nuclear LOSVD is presented by Gerssen, Kuijken, & Merrifield (1995), who obtained a spectrum with the Multiple Mirror Telescope in $\sim 1''$ seeing, using a $1''.25$ slit along PA 148° , or about 106° from the P1–P2 line. Within $\sim 1''$ of the brightest point along their slit, they detected an asymmetric positive-velocity tail to the LOSVD. Using a two-Gaussian decomposition, they interpret this tail as a discrete component with a mean velocity of $+160 \text{ km s}^{-1}$ (relative to systemic) and a dispersion $< 100 \text{ km s}^{-1}$, and identify it with P1. In our case, we do not see a clear signature of P1 as a separate kinematic component. Rather, P1 appears as a brightness enhancement along the generally smooth V and σ profiles. Nonetheless, Gerssen et al.’s basic result of an asymmetric LOSVD can be consistent with ours, depending on the centering of their slit. Merrifield (1998, private communication) reports that the slit was centered visually on the brightest point in the nucleus as seen on the slit-jaw TV. This implies that the slit center was probably near P1, though, given the slit width and seeing, an error of a couple of tenths of an arcsecond is not unlikely. Nominally, their slit would extend from about $-1''.1$ to $+0''.1$ on our scale, or displaced from the RC toward the positive-velocity side. A centering error of $0''.25$ in the direction away from P2 would put the RC at the edge of their slit, and positive velocities would dominate. Contrary to Gerssen et al.’s later comment, the LOSVD asymmetry does not rule out Tremaine’s (1995) eccentric disk model, since their slit would not have covered the entire disk, and the negative-velocity side of their observed LOSVD would be very sensitive to centering errors of this magnitude.

Our results are also broadly consistent with the nuclear major- and minor-axis V and σ profiles obtained by van der Marel et al. (1994) using the William Herschel Telescope ISIS spectrograph and the MMT Red Channel. Their major-axis rotation curve, obtained in $\sim 1''$ seeing, crosses zero $\sim 0''.2$ from the brightness maximum on their slit (which we identify as P1) in the direction towards P2. On the nuclear minor axis, on a slit also running through P1, they find $V \approx 50 \text{ km s}^{-1}$ at the brightest point. If their $0''.8$ slit were centered exactly on P1, we might have expected, based on the FOC rotation curve, a somewhat higher velocity; but seeing may have shifted the apparent brightness peak, and consequently their slit, slightly toward the RC. Their major-axis dispersion profile peaks within $0''.1$ of P2, as does our convolved profile in Figure 6.

Observations made at the CFHT with the TIGER integral-field spectrograph are reported by Bacon et al. (1994). Their spatial resolution was not quite as good as that of KB, but their data cover a two-dimensional field on the sky, roughly $10'' \times 8''$. The general behavior of the TIGER

kinematic fields in the direction perpendicular to our slit supports our above assumption of little variation in V and σ over the width of KB’s aperture. The TIGER rotation curve peaks roughly $0''.7$ from the RC at an amplitude of 120 km s^{-1} , which is entirely consistent with the FOC rotation curve convolved to a resolution slightly broader than in Figure 6. Puzzlingly, however, the TIGER dispersion field peaks at $+0''.73$ from P2,⁴ in the anti-P1 direction. We cannot confirm this result with the FOC data. While our σ values at $+0''.7$ are not especially trustworthy, we do see the dispersion falling steeply from the spike out to $0''.4$, and it is difficult to see how the apparent peak dispersion could be shifted that far if the true peak were at P2. We have no explanation for this discrepancy. We can remark, however, that Bacon et al. find the TIGER rotation center also on the anti-P1 side of P2, which the FOC data contradict.

5.2. Comparison with Published Models

There have been many efforts to model the central kinematics of M31, mainly with the goal of estimating the mass of the likely black hole (see Hodge 1992 and Kormendy & Richstone 1995 for reviews). However, only two published models to date deal quantitatively with the asymmetric structure of the nucleus, and we confine ourselves to a comparison with these models.

Emsellem & Combes (1997, hereafter EC) consider P1 to be a star cluster orbiting P2, the true center of the nucleus harboring the black hole. The cluster must be of sufficient density that it largely avoids tidal disruption up to the present time; but as a consequence dynamical friction rapidly brings the cluster in to a radius where it *is* disrupted. EC estimate that the present configuration will have a lifetime substantially under a million years, but also argue that nuclear ingestion of globular clusters should be a common event. EC present N -body simulations of a system consisting of a static bulge, an axisymmetric nuclear disk, a central dark mass of $9.4 \times 10^7 M_\odot$, and an orbiting cluster. They focus primarily on comparison with the TIGER data, but plot kinematic profiles for their best model at a resolution of $0''.06 \times 0''.06$, which is a fairly close match to our $0''.063$ slit width and $0''.056$ zoomed pixel scale. We plot these profiles, read directly from EC’s Figure 15, as the dotted lines in Figure 7, compared with our results. Possibly due to the desire to fit the TIGER data, their rotation curve crosses zero at about $+0''.1$ on the anti-P1 side of P2, which is not consistent with the FOC data. The velocity dispersion in the EC model is particularly low in P1, since it is assumed to be a bound cluster of only a few million M_\odot . We do not detect a low σ in P1, although we may have systematic errors in our dispersions, and even with higher S/N we would probably have difficulty measuring $\sigma \approx 60 \text{ km s}^{-1}$ as EC predict. EC’s dispersion reaches a maximum of 290 km s^{-1} $0''.25$ from P2, which is marginally consistent with, though qualitatively different from, our dispersion spike. Since EC did not do a systematic study of the parameter space, it is difficult to say whether their model could be adjusted to fit the

⁴Actually Bacon et al. set their origin at what they call the “nucleus photometric center,” which, from close inspection of their Figures 13 and 26, we identify with P2.

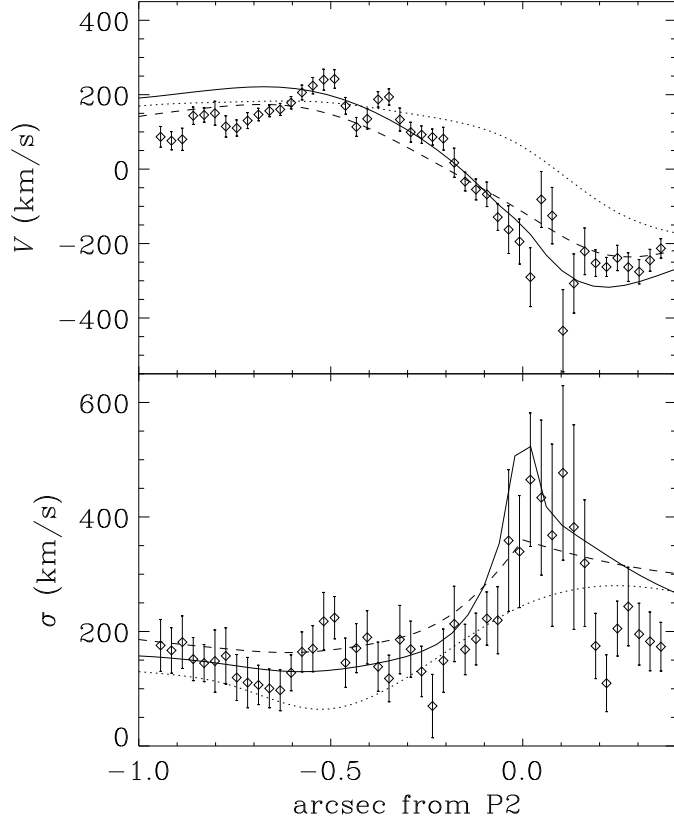


Fig. 7.— Comparison of the FOC kinematic profiles (*diamonds*) with dynamical models at *HST* resolution. *Dotted line*, sinking cluster model of Emsellem & Combes (1997). *Dashed line*, eccentric disk model of Tremaine (1995), scaled up by 20% in velocity. *Solid line*, modified Tremaine-like model (see Sec. 5.2).

dispersion spike and the rotation curve. However, the $\sim 200 \text{ km s}^{-1}$ dispersion we measure in P1, if confirmed by STIS, would argue strongly against P1 being a bound cluster, consistent with the argument of King et al. (1995) that the P1 colors indicate a metallicity substantially above that of typical globulars.

If P1 is not a bound object, it may still be produced by a statistical accumulation of stars, as in the model of Tremaine (1995). In this model P2 represents the stellar cusp associated with the black hole, around which orbits an eccentric Keplerian disk. The line of apsides in the disk is presumed straight or nearly so, and the brightness enhancement at P1 is caused by the accumulation of stars lingering near the apocenters of their orbits. In this picture P1 is a purely kinematic $m = 1$ density wave with zero pattern speed. It is necessary that the eccentricity of the disk decrease outwards, and also that its surface density decrease interior to P1, in order to produce a “blob” in projection rather than simply an extension of P2 or a ring around it. For the correct viewing

geometry, the rapid speeds of disk stars near pericenter place P2 at negative velocity in projection, shifting the RC toward P1, as we observe. Tremaine plots V and σ profiles for a model that fits the Lauer et al. (1993) photometry and groundbased kinematics from Kormendy (1988), both at groundbased and “perfect” resolution. We show the latter result as the dashed lines in Figure 7. We have scaled up the original model by 20% in velocity, or 9.5% in black-hole mass, to improve the fit. The agreement in the rotation curve is admirable, though the central slope is somewhat underestimated. The dispersion profile is consistent with our data except in the dispersion spike.

We have computed a number of Tremaine-like models to test whether the fit can be improved by minor tweaking of the parameters. An improved model is shown as the solid line in Figure 7. This model uses the same black-hole mass ($7.5 \times 10^7 M_\odot$) as Tremaine’s original model. We emphasize, however, that in neither case has the mass been treated as a free parameter; this discussion is *not* a measurement of the mass of the central object, only an illustration of the flexibility of the eccentric-disk picture. Our improved model has a slightly higher eccentricity and a steeper eccentricity gradient. In order to reproduce the dispersion spike and the rotation gradient at RC we have had to rotate the line of apsides so that it aligns with the line of nodes, with the result that the model does not reproduce the PA difference between the P1–P2 line and the nuclear major axis. It turns out to be rather difficult to reproduce simultaneously the steepness of the rotation curve, the location of the RC, and the overall photometric symmetry of the nucleus about P2 beyond the distance of P1. Higher eccentricity can sharpen the rotation curve but damages the photometric symmetry. The narrowness of the dispersion spike poses another problem. The line-of-sight dispersion can be kept low on the P1 side of the spike by the contribution of the cold disk component, which, on that side, rotates slowly along with the underlying inner bulge. On the anti-P1 side the disk is a minor contributor to the projected light, and furthermore is well separated in radial velocity from the bulge stars. As a result it is extremely difficult to reproduce the dispersion gradient on the anti-P1 side of the spike with a Tremaine-like model. It is conceivable that introducing rotation in the central part of the bulge component—which in the Tremaine model is non-rotating—could reduce the problem a bit. Alternatively, a very steep eccentricity gradient inward toward the inner edge of the disk could help, but this poses technical difficulties for the models as presently formulated.

The value of demanding a more exact fit from what is a *very* approximate model is dubious, however. Tremaine’s model, as published, contains many simplifying assumptions. The disk is assumed infinitely thin, and approximated by thin “ringlets”, broadened by a simple convolution in the plane of the sky. Velocity dispersion in the disk is not included in a realistic way. The self-gravity of the disk and the potential of the bulge are both ignored. In our models we have corrected only the decomposition into ringlets, adopting a continuous mass distribution. None of these approximations is a failing *per se*, since at groundbased resolution a rigorously careful treatment is not warranted. However, we are very near, if not at, the point where dynamical models of the M31 nucleus will require self-consistency in some measure to address more than just the gross characteristics of the data. Detailed modeling is beyond the scope of this paper, but we

hope to report on further modeling efforts in a future publication.

6. Summary

We have used the $f/48$ long-slit spectrograph of the *HST* Faint Object Camera to observe the double nucleus of M31 in the spectral region from 3670 \AA to 5500 \AA . We acquired a 19,000-sec. exposure with the slit oriented along the P1–P2 line. A calibration spectrum of Jupiter was used as a spectral template in a cross-correlation algorithm to extract the profiles of the projected mean velocity V and velocity dispersion σ . Though the analysis was complicated by detector backgrounds, geometrical distortions, and low signal-to-noise ratio, we believe the data convincingly show

1. a resolved rotation curve, with maximum amplitude $\sim 250\text{ km s}^{-1}$ and center (zero point) on the P1 side of P2; and
2. a generally low ($\lesssim 250\text{ km s}^{-1}$) dispersion everywhere except for a narrow “dispersion spike”, centered very close to P2, where σ peaks at $440 \pm 70\text{ km s}^{-1}$.

At lower confidence, there may be unresolved local disturbances to the rotation curve associated with P1 and P2, and a slight elevation in σ at P1. And at very low statistical significance we find a weak signature of LOSVD asymmetry that is opposite to that usually encountered, in the sense that the longer tail of the distribution is in the direction of rotation.

Our results are generally consistent with previous groundbased work. In particular, when we convolve our data to match the resolution of Kormendy & Bender’s (1999) CFHT/SIS data, we find an excellent agreement in the rotation curve, and a 20% disagreement in the dispersion profile that cannot be traced to the dispersion spike. Our V and σ profiles are consistent with the data of Gerssen et al. (1995) and van der Marel et al. (1994), although the latter authors do not detect the same sense of LOSVD asymmetry that we see. Our data are *not* consistent with certain details of the CFHT/TIGER data of Bacon et al. (1994), specifically the locations, relative to P2, of the rotation center and the maximum dispersion.

Finally, we have assessed the ability of two published models to fit the FOC data. The sinking star cluster model of Emsellem & Combes (1997) does not reproduce either the rotation curve or the dispersion profile. In particular, it places the center of the rotation curve on the wrong side of P2, and predicts that P1, being a bound, low-mass object, should have $\sigma \approx 60\text{ km s}^{-1}$, whereas we measure $\sigma \sim 170\text{ km s}^{-1}$. The eccentric disk model of Tremaine (1995) comes closer to matching the FOC profiles, if the central black hole mass is scaled up by 10%. A significant improvement to the kinematic fit can be realized by tweaking the parameters, at some sacrifice to the photometric fit. The models, however, are presently limited by simplifying assumptions that are less than realistic. Quantitative dynamical modeling of the M31 double nucleus will require models of significantly greater realism and sophistication, especially when data from STIS become available.

TSS acknowledges support from NASA Astrophysical Theory Program Grant NAG5-3050 and NSF CAREER grant AST-9703036, IRK from NASA Grant NAG5-1607, and PC from NASA Grant NAS5-27760. We thank John Kormendy for providing details of the CFHT/SIS observations in advance of publication, and Mike Merrifield and Marc Davis for useful information and helpful suggestions.

Appendix: Kinematic Data

Tables 1 and 2 present the derived kinematic profiles in the region between $-1''$ and $+0''.4$ from P2. Table 1 gives the results of the analysis on single-column spectra from the de-zoomed images (Fig. 3); some information is present on these scales because of the orbit-to-orbit positional shifts of the spectrum on the detector. Table 2 gives the results for columns summed in pairs, corresponding to the original zoomed pixel format (Fig. 4). Uncertainties include the systematic contribution from the choice of filter and fitting parameters in the cross-correlation code, but not from template mismatch or background corrections.

Table 1. M31 Nuclear Kinematics — De-Zoomed Pixel Resolution

$R(”)$	V	\pm	σ	\pm
−0.943	86.8	27.9	175.7	45.4
−0.915	76.3	24.4	166.9	39.7
−0.887	80.1	29.8	181.4	45.9
−0.858	143.5	23.3	151.8	37.7
−0.830	145.6	19.3	144.8	32.5
−0.802	150.2	32.2	148.3	54.4
−0.773	114.8	28.5	157.3	49.2
−0.745	110.4	21.8	119.6	40.1
−0.717	130.4	21.3	110.8	44.0
−0.688	146.6	16.8	106.7	34.4
−0.660	156.5	15.7	100.6	33.8
−0.632	160.4	16.1	97.4	35.9
−0.603	178.4	16.6	127.9	31.5
−0.575	206.0	19.9	164.4	35.0
−0.547	224.3	22.0	169.9	40.3
−0.518	240.3	28.2	217.9	50.4
−0.490	242.3	24.9	224.2	36.9
−0.462	170.2	22.4	145.4	43.0
−0.433	113.6	25.2	170.9	42.9
−0.405	135.2	27.4	189.8	46.5
−0.377	187.4	20.7	138.5	43.0
−0.348	193.9	21.9	118.0	40.7
−0.320	133.2	30.9	185.8	59.7
−0.292	99.4	26.7	169.0	49.0
−0.263	92.7	23.3	130.2	44.0
−0.235	86.3	21.4	69.8	55.3
−0.207	81.9	30.6	149.1	55.2
−0.178	17.2	39.1	213.2	65.9
−0.150	−33.3	25.2	168.6	44.1
−0.122	−54.6	28.1	186.9	45.2
−0.093	−67.7	32.9	222.6	46.5
−0.065	−129.0	35.7	219.7	58.6
−0.037	−162.6	64.0	358.9	123.8
−0.008	−194.6	60.4	339.6	97.8

Table 1—Continued

$R(")$	V	\pm	σ	\pm
0.020	−290.2	79.1	465.2	116.6
0.048	−81.4	75.1	433.8	135.3
0.076	−125.0	75.8	368.1	159.2
0.105	−434.3	110.6	476.9	152.5
0.133	−307.3	79.4	382.3	178.7
0.161	−220.9	62.6	319.3	110.6
0.190	−252.6	35.8	174.8	57.0
0.218	−262.7	25.6	109.7	49.7
0.246	−238.7	34.0	205.1	47.9
0.275	−263.2	38.6	243.6	68.7
0.303	−275.7	32.7	195.4	54.0
0.331	−244.9	29.4	182.7	51.4
0.360	−212.9	26.1	173.4	42.6

Table 2. M31 Nuclear Kinematics — Zoomed Pixel Resolution

$R(”)$	V	\pm	σ	\pm
−0.929	82.1	23.2	169.3	38.0
−0.872	117.3	23.0	161.3	37.3
−0.816	151.0	21.3	145.9	37.8
−0.759	111.9	23.0	139.9	38.4
−0.702	140.8	17.0	105.8	37.3
−0.646	159.0	14.5	100.4	31.3
−0.589	191.8	16.3	147.4	28.9
−0.532	229.8	22.5	197.7	39.7
−0.476	202.4	22.3	186.7	38.9
−0.419	123.2	23.7	177.9	39.6
−0.363	188.9	19.1	124.7	36.3
−0.306	116.0	26.3	178.6	49.3
−0.249	91.9	21.0	105.5	42.7
−0.193	57.3	31.2	179.0	48.5
−0.136	−43.2	23.4	177.9	40.6
−0.079	−95.0	32.1	230.4	44.4
−0.023	−177.5	49.3	354.1	78.8
0.034	−159.6	69.6	462.5	125.8
0.091	−190.9	70.4	370.6	146.0
0.147	−247.9	55.1	340.6	102.3
0.204	−256.4	27.0	139.6	45.6
0.261	−245.2	32.2	218.5	50.6
0.317	−259.4	27.1	189.4	45.7
0.374	−223.5	28.5	213.2	41.5

REFERENCES

Bacon, R., Emsellem, E., Monnet, G., & Nieto, J.-L. 1994, *A&A*, 281, 691

Emsellem, E., & Combes, F. 1997, *A&A*, 323, 674

Gerssen, J., Kuijken, K., & Merrifield, M. 1995, *MNRAS*, 277, L21

Ho, L. C., Filippenko, A. V., & Sargent, W. L. W. 1993, *ApJ*, 417, 63

Hodge, P. 1992, *The Andromeda Galaxy* (Dordrecht: Kluwer), Ch. 8

Jedrzejewski, R., & Voit, M. 1997, in 1997 HST Calibration Workshop, ed. S. Casertano, R. Jedrzejewski, T. Keyes, & M. Stevens (Baltimore: Space Telescope Science Institute), 413.

King, I. R., Stanford, S. A., & Crane, P. 1995, *AJ*, 109, 164

Kormendy, J. 1988, *ApJ*, 325, 128

Kormendy, J., & Bender, R. 1999, in preparation

Kormendy, J., & Richstone, D. 1995, *ARA&A*, 33, 581

Lallemand, A., Duchesne, M., & Walker, M. 1960, *PASP*, 72, 76

Lauer, T. R., Faber, S. M., Groth, E. J., Shaya, E. J., Campbell, B., Code, A., Currie, D. G., Baum, W. A., Ewald, S. P., Hester, J. J., Holtzman, J. A., Kristian, J., Light, R. M., & Westphal, J. A. 1993, *AJ*, 106, 1436

Lauer, T. R., Faber, S. M., Ajhar, E. A., Grillmair, C. J., & Scowen, P. A. 1998, submitted to *AJ*

Light, E., Danielson, R., & Schwarzschild, M. 1974, *ApJ*, 194, 257

Statler, T. S. 1995, *AJ*, 109, 1371

Tremaine, S. 1995, *AJ*, 110, 628

van der Marel, R. P., & Franx, M. 1993, *ApJ*, 407, 525

van der Marel, R. P., Rix, H.-W., Carter, D., Franx, M., White, S. D. M., & de Zeeuw, T. 1994, *MNRAS*, 268, 521

Voit, M. 1996, FOC Instrument Science Report OSG-FOC-097 (Baltimore: Space Telescope Science Institute)